Research Article

Ultrabroad band microwave absorption from hierarchical MoO₃/TiO₂/Mo₂TiC₂Tₓ hybrids via annealing treatment

Feiyue HU[a], Fan ZHANG[a], Xiaohan WANG[a], Yaya LI[a], Hailong WANG[a],
Rui ZHANG[a,b], Hongxia LI[c], Bingbing FAN[a,*]

[a]*School of Material Science and Engineering, Zhengzhou University, Zhengzhou 450001, China*
[b]*School of Materials Science and Engineering, Luoyang Institute of Science and Technology, Luoyang 471023, China*
[c]*Sinosteel Luoyang Institute of Refractories Research Co., Ltd., Luoyang 471039, China*

Abstract: Two-dimensional (2D) transition metal carbide MXene-based materials hold great potentials applied for new electromagnetic wave (EMW) absorbers. However, the application of MXenes in the field of electromagnetic wave absorption (EMA) is limited by the disadvantages of poor impedance matching, single loss mechanism, and easy oxidation. In this work, $MoO_3/TiO_2/Mo_2TiC_2T_x$ hybrids were prepared by the annealing-treated $Mo_2TiC_2T_x$ MXene and uniform MoO_3 and TiO_2 oxides *in-situ* grew on $Mo_2TiC_2T_x$ layers. At the annealing temperature of 300 ℃, the minimum reflection loss (RL_{min}) value of $MoO_3/TiO_2/Mo_2TiC_2T_x$ reaches −30.76 dB (2.3 mm) at 10.18 GHz with a significantly broadening effective absorption bandwidth (EAB) of 8.6 GHz (1.8 mm). The *in-situ* generated oxides creating numerous defects and heterogeneous interfaces enhance dipolar and interfacial polarizations and optimize the impedance matching of $Mo_2TiC_2T_x$. Considering the excellent overall performance, the $MoO_3/TiO_2/Mo_2TiC_2T_x$ hybrids can be a promising candidate for EMA.

Keywords: $MoO_3/TiO_2/Mo_2TiC_2T_x$ composites; $Mo_2TiC_2T_x$ MXene; electromagnetic wave absorption (EMA); impedance matching; interfacial polarization; dielectric loss

1　Introduction

At present, the problems of electromagnetic wave (EMW) leakage and mutual interference are gradually becoming more complicated and serious, which not only affects the operation of communication equipment, but also endangers human health [1–3]. The development of new high-performance electromagnetic wave absorption (EMA) materials is an important approach to solve

such problems. Two-dimensional (2D) transition-metal carbides (MXenes) have abundant chemically active sites, various functional groups, and other characteristics, becoming a promising candidate in the EMA field [4,5].

In 2016, Qing *et al.* [6] first discovered that $Ti_3C_2T_x$ nanosheets have microwave absorption properties with a reflection loss (RL) value of −17 dB. The studies have shown that different etching time, etchant concentrations, etching temperatures, and the mixing ratios of $Ti_3C_2T_x$ nanosheets and paraffin wax can affect the microwave absorption properties of $Ti_3C_2T_x$ nanosheets [7]. However, the absorbing performance of MXenes alone still

---

* Corresponding author.
E-mail: fanbingbing@zzu.edu.cn

cannot meet the requirements of modern wave-absorbing materials due to their single loss mechanism, impedance mismatch caused by high complex permittivity and low complex permeability, and susceptibility to oxidation [8,9].

To solve the mentioned drawbacks, the research focused on compounding MXene with magnetic substances to optimize impedance matching and enhance magnetic loss, preparing MXene with carbon materials or conducting polymers to enhance dielectric loss, and exploring new MXenes and their composites other than $Ti_3C_2T_x$ for EMA applications [10–12]. Very recently, we have reported a new double transition metal MXene with excellent EMA properties, named $Mo_2TiC_2T_x$, where the Mo atoms hold the outer layers, and the Ti atoms load the middle layers compared to $Ti_3C_2T_x$ [13]. Nevertheless, the narrow effective absorption bandwidth (EAB) and the common RL intensity of pure $Mo_2TiC_2T_x$ limit its application in the field of EMA. It has been shown that the introduction of oxides can modulate the impedance matching situation of MXenes, while increasing the number of heterogeneous interfaces, thus enhancing the interfacial polarization losses [14]. Fan *et al*. [15] also proved that the 2D-layered Ti_3C_2/TiO_2 hybrids are expected to exhibit the enhanced EMA performance thanks to the appropriate complex permittivity, matching impendence, and high dielectric loss due to the introduction of TiO_2 oxides.

In this work, $MoO_3/TiO_2/Mo_2TiC_2T_x$ composites with different oxidation levels were obtained by annealing treatment on the multilayer $Mo_2TiC_2T_x$ (m-$Mo_2TiC_2T_x$) powders. A large number of heterogeneous interfaces generated by MoO_3 and TiO_2 were successfully introduced into 2D m-$Mo_2TiC_2T_x$ to construct 0D/2D heterogeneous structures. Meanwhile, MoO_3 and TiO_2 can optimize the impedance matching of $Mo_2TiC_2T_x$ MXene, which greatly increases the EAB of $Mo_2TiC_2T_x$ MXene. Obviously, it is a very promising broadband absorbing material, which is worthy of further research and application.

2 Experimental

2. 1 Materials and reagents

Mo_2TiAlC_2 powders ($\geqslant$ 99% purity, 200 mesh) were bought from 11 Technology Co., Ltd., China. Hydrofluoric acid (HF) ($\geqslant$ 49 wt%) and absolute ethanol were purchased from Shanghai Macklin Biochemical Co., Ltd. (Shanghai, China). All the chemicals are analytical grade, commercially available, and used without further treatment. The deionized water used in this work was provided by an ultra-pure water purification facility.

2. 2 Synthesis of m-$Mo_2TiC_2T_x$ MXene

The m-$Mo_2TiC_2T_x$ was prepared by the conventional acid etching method. Briefly, 2 g of Mo_2TiAlC_2 ceramic powders were slowly added in 40 mL of highly concentrated HF solution ($\geqslant$ 49 wt%). The whole process was in a 100-mL Teflon beaker at 50 ℃ and magnetic stirring for 48 h. The mixture was centrifugally washed with deionized water until pH ≈ 6. The precipitate was collected and vacuum-dried at 50 ℃ for 12 h to obtain m-$Mo_2TiC_2T_x$ MXene powders.

2. 3 Synthesis of $MoO_3/TiO_2/Mo_2TiC_2T_x$ hybrids

0.3 g m-$Mo_2TiC_2T_x$ MXene powders were placed in a 30-mL alumina crucible and spread out fully with a lid. The $Mo_2TiC_2T_x$ MXene powders experienced the annealing in a muffle furnace, and the temperature was set to 100 ℃ with a rate of 5 ℃/min for 2 h. The powders were cooled down to room temperature and labeled as T1. Similarly, the samples were labeled as T2, T3, T4, and T5 at the setting temperatures of 200, 300, 400, and 500 ℃, respectively.

2. 4 Characterization

The crystal structures of the as-prepared samples were indicated by the X-ray diffractometer (XRD; D/max-3C, Rigaku, Japan) equipped with a Cu Kα radiation source (λ = 0.15418 nm) at 40 kV, with scanning angles (2θ) of 5°–90°. The electron dispersive spectroscopy (EDS) mappings and surface micromorphology images of the hybrid materials were observed using a field emission scanning electron microscope (FE-SEM; JEOL, JSM-7001F, Japan). The transmission electron microscope (TEM; JEOL, JEM-2100F, Japan) provided microscopic morphologies of the samples and high-resolution transmission electron microscopy (HRTEM) images and selected area electron diffraction (SAED) patterns. The X-ray photoelectron spectrometer (ESCALAB 250Xi K-Alpha, Thermo Fisher Scientific, USA) was used to analyze the surface chemical information of the 2D $MoO_3/TiO_2/Mo_2TiC_2T_x$ composites. All the high-resolution spectra were corrected by shifting the C 1s peak at 284.5 eV.

2. 5 EMA measurements

In this study, the electromagnetic parameters of the synthesized samples were tested by the means of a vector network analyzer (5234A, Agilent, USA) using the coaxial line method. All the samples were then tested by mixing and melting the samples with paraffin wax in a mass ratio of 6:4, followed by pressing into rings (inner diameter of 3.04 mm, outer diameter of 7.00 mm) using a customized mold. The electromagnetic parameters (ε_r, μ_r) of the absorbing rings are measured in a selected test mode at frequencies from 2 to 18 GHz, and the EMA performance of the sample is finally evaluated.

3 Results and discussion

3. 1 Characterization of $Mo_2TiC_2T_x$ and $MoO_3/TiO_2/Mo_2TiC_2T_x$

The preparation process of $MoO_3/TiO_2/Mo_2TiC_2T_x$ hybrids is shown in Fig. 1. First, $m-Mo_2TiC_2T_x$ was synthesized by selectively removing the Al layer from the parent Mo_2TiAlC_2 MAX phase via the aggressive HF etching process, during which the functional groups such as –O, –OH, and –F were decorated. Subsequently, the annealing treatment of $m-Mo_2TiC_2T_x$ powders was to obtain $MoO_3/TiO_2/Mo_2TiC_2T_x$ hybrids with different oxidation levels. As $m-Mo_2TiC_2T_x$ was exposed in hot air at the various setting temperatures, the functional groups on the surface of the nanosheets were replaced by –O groups, and then Mo and Ti atoms were oxidized and *in-situ* generated MoO_3 and TiO_2 on $m-Mo_2TiC_2T_x$ layers.

Figures 2(a)–2(d) exhibit the SEM images of Mo_2TiAlC_2, $Mo_2TiC_2T_x$, and $MoO_3/TiO_2/Mo_2TiC_2T_x$
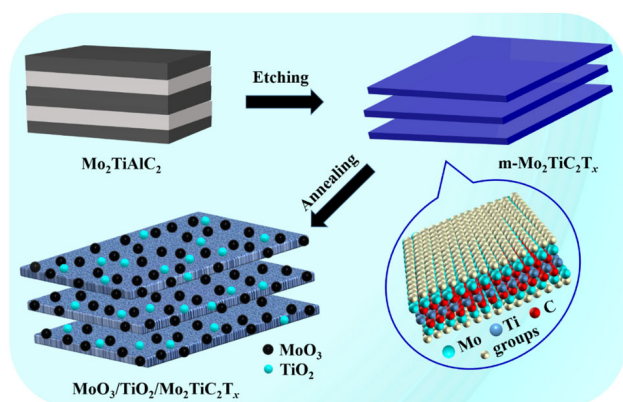
Fig. 1 Schematic diagram of the preparation of $MoO_3/TiO_2/Mo_2TiC_2T_x$ hybrids.
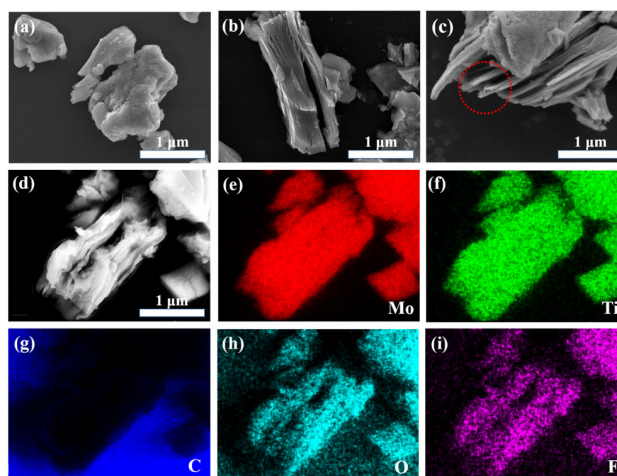
Fig. 2 SEM images of (a) Mo_2TiAlC_2, (b) $m-Mo_2TiC_2T_x$, (c) T2, and (d) T3. (e–i) EDS mappings of $MoO_3/TiO_2/Mo_2TiC_2T_x$ MXene (T3) corresponding to (d).

composites. The Mo_2TiAlC_2 MAX phase shows a tightly-packed laminar structure. The $Mo_2TiC_2T_x$ MXene after etching Mo_2TiAlC_2 MAX with high concentration of HF acid is shown in Fig. 2(b). The prepared sample shows a 2D lamellar structure due to the dissolution of the Al atomic layer by the acid, and the Ti–Al metal bonds are replaced by hydrogen bonds or van der Waals forces [16]. In Fig. S1(a) in the Electronic Supplementary Material (ESM), the delamination of T1 is more uniform compared to $m-Mo_2TiC_2T_x$ MXene. While the interlayer space of T2 is greatly enlarged to nearly 300 nm, as marked with the red circle in Fig. 2(c). Figure S1(b) in the ESM displays that the interlayer and surface of the $Mo_2TiC_2T_x$ MXene are covered by fine oxides after annealing at 300 ℃, resulting in the roughness and increased thickness of the lamellae, which more visually demonstrates that the $MoO_3/TiO_2/Mo_2TiC_2T_x$ hybrids were generated. When the temperature is increased to 400 ℃ (Fig. S1(c) in the ESM), the lamellae of MXene are further opened, showing a more scattered layered state. Figure S1(d) in the ESM shows that the surface of T5 is covered by dense and fine oxide spheres, and its interlayer is fully filled, indicating that $Mo_2TiC_2T_x$ MXene is highly oxidized at the annealing temperature of 500 ℃.

To further observe the element distributions in the sample, the EDS mappings of T3 were snapped, as shown in Figs. 2(e)–2(i). The layered structure of T3 can be observed from Fig. 2(d). In the EDS mappings, it can be observed that the co-existence of Mo, Ti, C, O, and F elements uniformly distributed in $MoO_3/TiO_2/Mo_2TiC_2T_x$ composites, confirming the feasibility of

acid etching and annealing treatment for the synthesis of this type of 2D MXene-based hybrids.

Figure 3(a) shows the X-ray diffraction (XRD) patterns of Mo_2TiAlC_2 MAX, $Mo_2TiC_2T_x$ MXene, and $MoO_3/TiO_2/Mo_2TiC_2T_x$ hybrids obtained by the annealing treatment. The XRD data of m-$Mo_2TiC_2T_x$ are consistent with the previously reported X-ray diffraction data of $Mo_2TiC_2T_x$ MXene, indicating that $Mo_2TiC_2T_x$ MXene was successfully delaminated during the HF etching process [17]. With the increase of annealing temperature, the (002) diffraction peak of $Mo_2TiC_2T_x$ gradually shifts to a lower angle, as shown in Fig. S2 in the ESM. The crystallographic d-spacing value of the (002) crystal plane of Mo_2TiAlC_2 is 0.926 nm ($2\theta = 9.54°$). Experienced the annealing process, the d-spacing values of the (002) peaks of $Mo_2TiC_2T_x$, T1, T2, and T3 increase to 1.064 nm ($2\theta = 8.33°$), 1.108 nm ($2\theta = 7.94°$), 1.161 nm ($2\theta = 7.59°$), and 1.254 nm ($2\theta = 7.04°$), respectively, indicating that the generated oxides further increase the crystalline spacing of the layered MXene [18]. Meanwhile, the (002) peak disappears at 400 ℃, and the (020) peak of MoO_3 appeared at 500 ℃ ($2\theta = 12.74°$, JCPDS No. 47-1320). T1–T5 show diffraction peaks of anatase TiO_2 at $2\theta = 37.64°$ and $2\theta = 38.70°$ compared to $Mo_2TiC_2T_x$, corresponding to the (004) and (112) crystal planes, respectively (JCPDS No. 21-1272) [15]. In addition, the characteristic peaks of $Mo_2TiC_2T_x$ at 30°–40° gradually decrease and even disappear, and in contrast, the diffraction peaks of MoO_3 (plum marker) and TiO_2 (square sheet marker) show up, further indicating that the oxides are *in-situ* generated on the basis of $Mo_2TiC_2T_x$ MXene, and the layered hybrids are obtained.

Figures 3(b)–3(e) show that the prepared $MoO_3/TiO_2/Mo_2TiC_2T_x$ (T3) was examined by the TEM, HRTEM, and SAED to further describe its morphology and structure. As depicted in the TEM image in Fig. 3(b), $MoO_3/TiO_2/Mo_2TiC_2T_x$ is composed of multiple lamellar layers, and the bright gaps are favorable illustrations of the layers being opened, demonstrating the typical lamellar structure and cross-sectional shear–slip morphology of MXene. Unlike the unannealed m-$Mo_2TiC_2T_x$ MXene, T3 has a rougher surface, and the layer stacking phenomenon is more scattered, indicating that the lamellar structure of $Mo_2TiC_2T_x$ is further opened at 300 ℃ with *in-situ* growth of oxides at its surface and interlayer. Figure 3(c) is an enlarged view of the edge of Fig. 3(b). Black area on the right is the $Mo_2TiC_2T_x$ matrix, and light gray on the left is the oxide, which has a thickness of about 50 nm. As shown in Fig. 3(d), an HRTEM image was performed for the above location, and its left part shows a lattice stripe spacing of 0.203 nm, which corresponds to the (200) crystal plane of MoO_3, indicating that the oxide is MoO_3. Additionally, the right part shows a lattice stripe spacing of 0.462 nm, which corresponds to the crystallographic spacing of the (006) crystal plane of $Mo_2TiC_2T_x$ MXene [19]. Meanwhile, its diffraction rings are observed by the SAED mode in Fig. 3(e), indicating that the prepared $MoO_3/TiO_2/Mo_2TiC_2T_x$ material has a polycrystalline structure. The formation of multilayer $MoO_3/TiO_2/Mo_2TiC_2T_x$ was confirmed from the above TEM analysis.

The X-ray photoelectron spectroscopy (XPS) was used to explore the surface chemical states of $Mo_2TiC_2T_x$ MXene and $MoO_3/TiO_2/Mo_2TiC_2T_x$ (T3). The binding energies in the XPS spectra depicted in Fig. 4 are
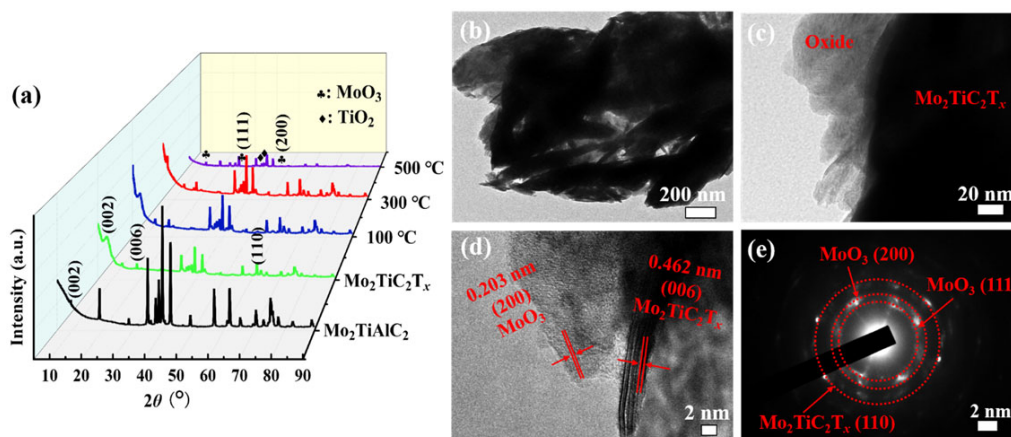
Fig. 3 (a) XRD patterns, (b, c) TEM images, (d) HRTEM image, and (e) SAED pattern of $MoO_3/TiO_2/Mo_2TiC_2T_x$ composit annealing treated at 300 ℃.
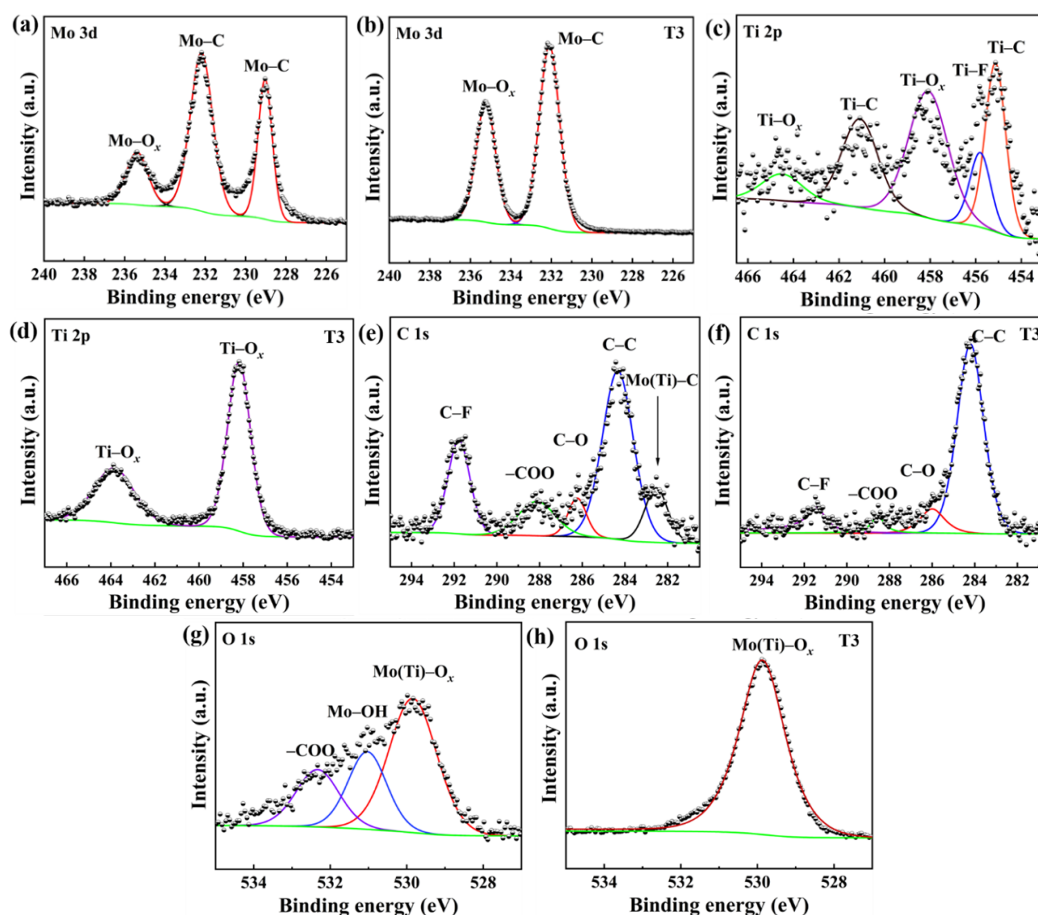
Fig. 4 Comparative XPS spectra between $Mo_2TiC_2T_x$ MXene and $MoO_3/TiO_2/Mo_2TiC_2T_x$ composites (T3): high-resolution (a, b) Mo 3d, (c, d) Ti 2p, (e, f) C 1s, and (g, h) O 1s spectra.

calibrated to the binding energy of C 1s (284.5 eV). Figure S3 in the ESM shows the full XPS spectra of $Mo_2TiC_2T_x$ and T3, where the binding energy peaks corresponding to the signals of Mo, Ti, C, O, and F elements are observed. To further compare the changes of surface chemical information from these elements, the high-resolution XPS spectra of Mo 3d, Ti 2p, C 1s and O 1s were given. From the Mo 3d spectra in Figs. 4(a) and 4(b), it can be found that $Mo_2TiC_2T_x$ has three peaks corresponding to Mo–C, Mo–C, and Mo–O_x (MoO_3) bonds at 229.1, 232.2, and 235.4 eV [20], respectively. While the MoO_3 peak (235.2 eV) of the T3 is more prominent, only one Mo–C peak (232.1 eV) is present, indicating that partial oxidation of $Mo_2TiC_2T_x$ has occurred at 300 ℃.

Figures 4(c) and 4(d) show the Ti 2p spectra of $Mo_2TiC_2T_x$ and T3. For the T3, the Ti–O_x peaks corresponding to 458.2 eV and 463.9 eV are the most prominent because the TiO_2 generated by annealing oxidation is distributed on the surface and edges of $Mo_2TiC_2T_x$, which is easy to be detected [21]. In

addition, $Mo_2TiC_2T_x$ also has three Ti-related fitted peaks, which correspond to two Ti–C peaks and one Ti–F peak at 455.1, 461.1, and 455.9 eV [22]. Meanwhile, no Ti–Al bond was found, indicating that the Al atoms were etched by the HF solution.

The C 1s spectrum of Fig. 4(e) shows deconvoluted peaks of $Mo_2TiC_2T_x$ at 282.5, 284.3, 286.3, 288.1, and 291.8 eV, which correspond to Mo(Ti)–C, C–C, C–O, –COO, and C–F bonds, respectively [23]. The presence of C–C may come from external contaminating carbon or Mo(Ti)–C structure. Additionally, the C–F bond originates from the fluorine functional group on the surface of MXene, and the oxygen-containing chemical bond is related to the oxygen in air. On the one hand, the disappearance of Mo(Ti)–C in T3 is due to the destruction of Mo(Ti)–C bond by oxidation reaction. On the other hand, $Mo_2TiC_2T_x$ is covered by oxide spheres, and Mo(Ti)–C bond is difficult to be detected (Fig. 4(f)). Moreover, the intensity of the C–F peak in T3 is reduced because the *in-situ* generated MoO_3 and TiO_2 occupy or cover the functional groups

on the MXene surface.

Figure 4(g) shows the O 1s spectrum of $Mo_2TiC_2T_x$, containing three characteristic peaks corresponding to $Mo(Ti)–O_x$ (529.8 eV), Mo–OH (531.1 eV), and –COO (532.4 eV) [24,25]. Meanwhile, Fig. 4(h) shows the O 1s spectrum of T3, and it can be found that $Mo_2TiC_2T_x$ has only one peak left after annealing treatment, which is $Mo(Ti)–O_x$ (529.9 eV), indicating that MoO_3 and TiO_2 cover the MXene surface more adequately at this time. The above XPS analyses reveal the surface chemical information of $Mo_2TiC_2T_x$ and $MoO_3/TiO_2/Mo_2TiC_2T_x$, demonstrating that the *in-situ* generated MXene-based hybrids were successfully obtained by a simple annealing treatment of m-$Mo_2TiC_2T_x$.

3. 2 EMA properties

It is well known that the EMA properties of materials are related to their relative permittivity and complex permeability. The real part of dielectric constant (ε') and the real part of complex permeability (μ') symbolize the ability of storing EMWs, while the imaginary part of dielectric constant (ε'') and the imaginary part of permeability (μ'') symbolize the ability of losing the incident waves [26]. In fact, since there are no magnetic elements in the prepared $MoO_3/TiO_2/Mo_2TiC_2T_x$, the μ' and μ'' values are close to 1 and 0, respectively.

To investigate the EMA properties of $MoO_3/TiO_2/Mo_2TiC_2T_x$ samples treated at different annealing temperatures, 60 wt% samples were mixed homogeneously with refined paraffin wax and tested from 2 to 18 GHz. Figures 5(a) and 5(b) show the ε' and ε'' of the $MoO_3/TiO_2/Mo_2TiC_2T_x$ samples (T1–T5) in the frequency range from 2 to 18 GHz. It can be seen that the values of ε' are in the range of 4–9, while the values of ε'' are between 0 and 2. Meanwhile, the values of ε' and ε'' of T3 compared to the other specimens are the highest, presumably due to the optimal content of generated oxides at the annealing temperature of 300 ℃. Moreover,

there are many fluctuation peaks at high frequencies (8–18 GHz) at the ε'–frequency (f) and ε''–f bends from T1 to T5, which are mainly caused by nonlinear dielectric resonances due to different polarizations [27].

The ε'' values of the samples (T1–T3) fluctuate widely, and two relatively obvious dielectric response peaks appear. Normally, for dielectric lossy EMW absorbing materials, the number of dielectric response peaks corresponds to the number of polarization behaviors, indicating the existence of multiple typical polarization modes for T1–T3 materials. According to the free electron theory [28]:

$$\varepsilon'' \approx \frac{\sigma}{2\pi f \varepsilon_0} \tag{1}$$

where σ is the electrical conductivity and ε_0 is the vacuum dielectric constant. The ε'' value is positively correlated with the value of electrical conductivity. As the loading of MoO_3 and TiO_2 increases, the ε'' values of T4 and T5 samples decrease, indicating that the electrical conductivity of the composites becomes worse. In addition, the tangent loss (tanδ) represents the loss performance of the EMW. Figure 5(c) shows the tanδ_ε (tan$\delta_\varepsilon = \varepsilon''/\varepsilon'$) for these sample/paraffin mixtures. The tanδ_ε values of T1–T3 samples at 10–18 GHz are larger than those of T4 and T5, indicating that the annealing at too high temperatures reduces the EMW loss characteristics. According to the Debye theory [29], tanδ_ε is related to the interfacial polarization and dipole polarization. At an annealing temperature of 300 ℃, the heterogeneous interfaces and defects in the hybrid material reach saturation, and the generated dielectric loss reaches the maximum. After that, too high annealing temperatures produce excessive oxides that coat the surface and interlayer of MXene, reducing the EMW propagation path and current transmission discontinuity inside the material.

Generally speaking, to evaluate the EMA properties
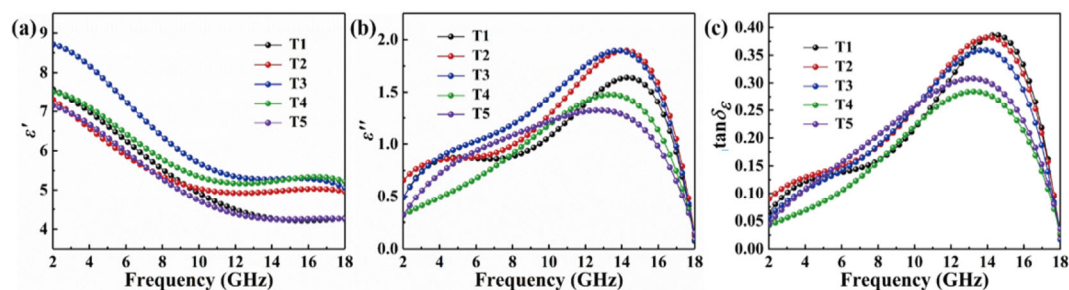
Fig. 5 (a) ε' and (b) ε'' of the complex permittivity, (c) dielectric tangent loss (tanδ_ε) of $MoO_3/TiO_2/Mo_2TiC_2T_x$ composites at various annealing temperatures.

of a material, three components should be considered: the minimum reflection loss (RL_{min}), the EAB, and the absorption coating thickness (d) [30]. In order to measure the actual EMA capability of the sample, refined paraffin wax was chosen as the matrix frame. Since the paraffin matrix is fully permeable to EMW, the results obtained by the vector network analyzer are considered as the EMA capability of the absorber itself. The EMA properties of the as-obtained products are affirmed by the RL value agreeing to the transmission line hypothesis, which can be evaluated by the relationship of ε_r and μ_r as demonstrated [31]:

$$RL = 20 \log \left| \frac{Z_{in} - Z_0}{Z_{in} + Z_0} \right| \qquad (2)$$

$$Z_{in} = Z_0 \sqrt{\mu_r / \varepsilon_r} \tanh \left(j \left(\frac{2\pi fd}{c} \right) \sqrt{\mu_r \varepsilon_r} \right) \qquad (3)$$

where c, f, ε_r, μ_r, Z_{in}, and Z_0 are the speed of light, the frequency of EMW, the complex permittivity, the complex permeability, the input characteristic impedance, and the impedance of free space, respectively.

The RL–frequency curves of T1–T5 samples in the range of 2–18 GHz for different thicknesses are shown in Fig. S4 in the ESM. As the oxidation level increases, $MoO_3/TiO_2/Mo_2TiC_2T_x$ hybrids exhibit different EMA characteristics. In terms of the RL value, T3 has the best RL_{min} value, reaching −30.76 dB (2.3 mm) at 10.18 GHz, whereas −19.16 dB (2.4 mm) at 10.52 GHz, −25.23 dB (2.3 mm) at 11.88 GHz, −20.30 dB (2.3 mm) at 10.86 GHz, and −27.43 dB (5 mm) at 17.32 GHz for

T1, T2, T4, and T5, respectively. Figure S4(f) in the ESM shows the RL curves of all the samples at the same thickness of 2 mm, and it can be found that T3 has the best RL_{min} value of −21.74 dB, implying that it has the best absorption performance, which may be attributed to the optimal interfacial polarization effect of $MoO_3/TiO_2/Mo_2TiC_2T_x$ prepared at 300 ℃. When the temperature is higher, the excess oxides will reduce the dielectric loss capability of this composite.

The current bottlenecks of MXene-based composites in the field of EMW absorption are mainly the problems of narrow absorption band and easy oxidation [32]. Based on this situation, the EAB can be analyzed with the help of more comprehensive three-dimensional (3D) RL mappings. Figures 6(a)–6(e) show the 3D absorption plots for T1 to T5, from which it can be seen that the EAB reaches 8.6 GHz (7.2–15.8 GHz) for T1 at 2.4 mm, 8.1 GHz (7.5–15.6 GHz) for T2 at 2.3 mm, 8.6 GHz (9–17.6 GHz) for T3 at 1.8 mm, 7.5 GHz (7.4–14.9 GHz) for T4 at 2.3 mm, and 7.4 GHz (7.5–14.9 GHz) for T5 at 2.5 mm. In summary, T3 achieves an absorption band of 8.6 GHz at a thinner thickness (1.8 mm) and has the best RL_{min} value (−30.76 dB) at a thickness of 2.3 mm (Fig. 6(f)). The effective absorption of EMW at frequencies from 4 to 18 GHz can be achieved by adjusting the coating thickness from 1 to 5 mm, making it a prominent EMA material. In terms of application, even the $MoO_3/TiO_2/Mo_2TiC_2T_x$ prepared by annealing at 500 ℃ has an EAB value of 7.4 GHz (2.5 mm), which illustrates the significance of this study.

Furthermore, we made a comprehensive comparison
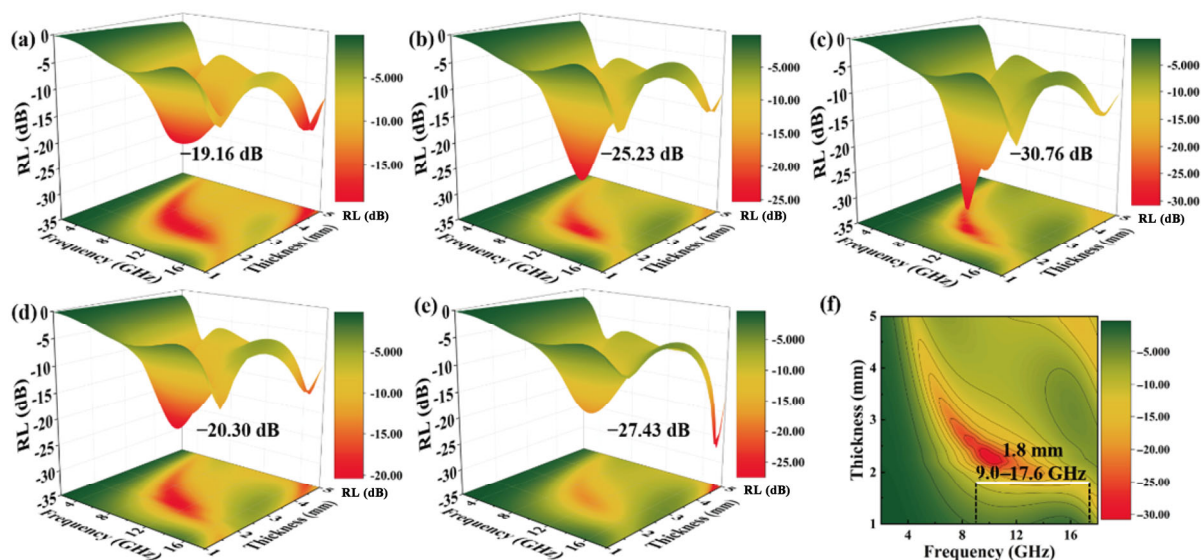
Fig. 6   3D plots of the RL of (a) T1, (b) T2, (c) T3, (d) T4, and (e) T5 in the paraffin matrix. (f) 2D representations of RL connected with different thicknesses of T3.

of the absorbing properties of T3 with the existing MXene-based composites, as listed in Table 1. It was found that the annealed T3 greatly broadened the absorbing band of $Mo_2TiC_2T_x$ and also had the advantage of wide band compared with $Ti_3C_2T_x$-based absorbing materials, demonstrating that it is a very outstanding EMA material.

3.3 EMA mechanism of $MoO_3/TiO_2/Mo_2TiC_2T_x$

It is well known that the two main indicators for assessing the EMA properties of materials are more EMWs into the material (impedance matching) and more losses of incident EMWs by the material itself (electromagnetic loss capability). Based on these, the EMA mechanism of layered $MoO_3/TiO_2/Mo_2TiC_2T_x$ hybrids were further investigated.

3.3.1 *Well matched impedance and multiple scattering by 0D/2D heterojunction*

A well-matched impedance situation is a prerequisite for the dissipation of the incident waves. To achieve zero EMW reflection at the air–absorber interface, the impedance condition of the absorber (Z_{in}) should be equal to that of free space (Z_0), i.e., $Z = Z_{in}/Z_0 = 1$ [39]. Figures S5(a)–S5(e) in the ESM show the plots of impedance matching values vs. thicknesses and frequencies for the T1–T5 samples. It can be seen that the maximum values of impedance matching (Z_{max}) for all the samples occur at a 5-mm thickness, and the lowest Z_{max} value is 1.91 (4.06 GHz) for T3, while the Z_{max} values of all the other samples exceed 2. Figure S5(f) in the ESM shows the impedance matching degree (Z)

Table 1 Electromagnetic assimilation properties of comparative absorbers

Sample	RL_{min} (dB)	d (mm)	EAB (GHz)	Ref.
Ti_3C_2 nanosheet	−17.0	1.4	6.0	[6]
$Ti_3C_2T_x$	−27.5	4.0	3.0	[33]
Annealed $Ti_3C_2T_x$	−48.4	1.7	2.8	[34]
Ni@MXene	−52.6	3.0	3.7	[35]
MXene/PI aerogel	−41.8	4.0	6.5	[32]
$MoS_2/TiO_2/Ti_3C_2T_x$	−33.5	1.0	3.1	[36]
$NiS/MoS_2/Ti_3C_2T_x$	−58.4	2.4	5.0	[37]
$NiCo/CeO_2/Ti_3C_2T_x$	−42.2	2.0	6.3	[30]
$Ni(NiO)/Ti_3C_2T_x/TiO_2$	−41.7	1.3	3.2	[38]
$Mo_2TiC_2T_x$	−25.3	1.6	3.2	[13]
$Ni/Mo_2TiC_2T_x$	−50.3	1.4	3.0	[24]
$MoO_3/TiO_2/Mo_2TiC_2T_x$	−30.7	2.3	8.6	This work

values for all the samples at the same thickness of 2 mm, and it can be found that the Z value of T3 is the smallest in the range of 2–18 GHz. At the same time, T3 has the widest frequency range of Z values near 1, indicating that the hybrid material prepared at 300 ℃ optimizes the impedance matching situation.

In order to investigate the intrinsic connection between impedance matching and absorbing performance more comprehensively and deeply, Fig. 7 was further plotted. Figures 7(a)–7(c) show the RL–frequency plots of T3 and the corresponding thickness simulations and impedance matching, and it can be found that the thickness of absorber simulated by different thicknesses of RL_{min} value can regulate the effective absorbing frequency band, and its corresponding frequency decreases with the increase of material thickness, which is consistent with the quarter-wavelength principle [40]. In Fig. 7(d), the best RL value of T3 is compared with Z value of the same thickness, and it can be found that the EAB at this thickness (7–15.2 GHz) and Z in the interval of 0.8–1.2 (6.5–15.1 GHz) fit very well, further illustrating the importance of impedance matching optimization as a guide to better design the EMA materials [41].

Figures 7(e) and 7(f) show the 3D plot of Z values and the 2D mapping plot vs. frequency, respectively, allowing a more comprehensive observation of the specific range of Z values of the T3 samples with thickness and frequency. It can be found that the Z value of T3 is close to the 0.8–1.2 range or even 1 in the thickness of 2 mm, and the Z value does not exceed 2 in the thickness of 1–5 mm, which proves that this 0D/2D structure has good impedance matching. Meanwhile, the classical multilayer structure of MXene increases the scattering and reflection of the incident wave between the sheets, which increases the wave propagation path and facilitates the effective attenuation of EMW.
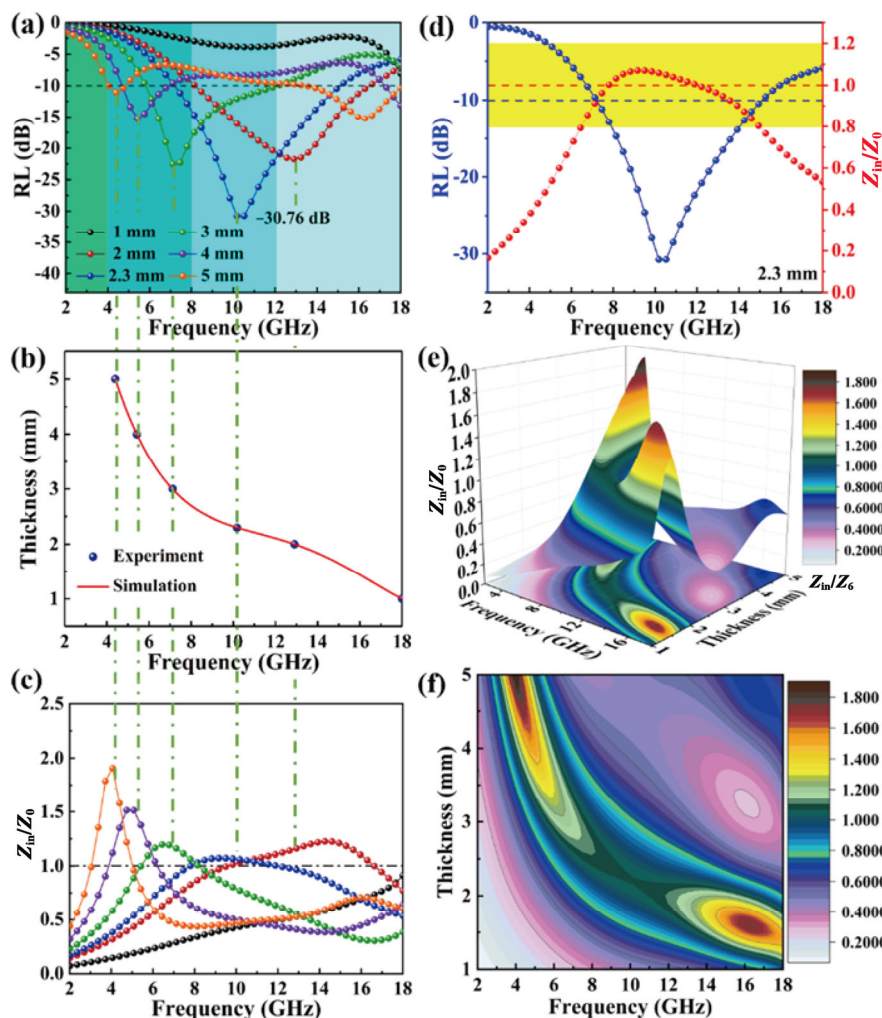
3.3.2 *Enhanced dielectric loss due to in-situ generated interfaces and defects*

The conducting chains or localized conducting networks in MXene nanosheets provide multiple channels for carrier migration and hopping. In the presence of an applied electric field, the $MoO_3/TiO_2/Mo_2TiC_2T_x$ medium is internally polarized, and the intensity vector of its polarization lags behind that of the electric field, leading to the generation of current. In this case, electrical energy is converted into heat by the material, thus increasing the conduction loss [42].

Fig. 7 (a) RL curves of T3, (b) relationship between the simulation thickness and peak frequency, (c) impedance matching rates (Z_{in}/Z_0) of T3, (d) relationship between RL_{min} and Z_{in}/Z_0 of T3 at a 2.3-mm thickness, (e) 3D plot of Z_{in}/Z_0 of T3, and (f) 2D representations of Z_{in}/Z_0 of T3.

In general, the relaxation process described by the Cole–Cole semicircle can explain the dielectric loss behavior of these materials. On the basis of Debye relaxation theory, if the relationship between ε' and ε'' is drawn, it can be found that there are some semicircles, and then each semicircle is associated with a Debye relaxation process, as shown in Eq. (4) [43]:

$$\left(\varepsilon' - \frac{\varepsilon_s - \varepsilon_\infty}{2}\right)^2 + \left(\varepsilon''\right)^2 = \left(\frac{\varepsilon_s - \varepsilon_\infty}{2}\right)^2 \quad (4)$$

where ε_s is the static permittivity and ε_∞ is the relative dielectric permittivity at the high-frequency limit.

As shown in Figs. 8(a)–8(e), semicircles in the Cole–Cole plots of T1–T5 samples indicate that the absorption mechanism of $MoO_3/TiO_2/Mo_2TiC_2T_x$ can be described by the Debye dielectric relaxation model. Meanwhile, there are two main sources of dielectric

loss in these materials: dipolar polarization and interfacial polarization [44]. Firstly, the abundant functional groups and defects on the surface of $Mo_2TiC_2T_x$ after acid etching can act as polarization centers to produce extremely strong dipole polarization effects. Secondly, the *in-situ* generation of oxides on MXene nanosheets brings a large number of heterogeneous interfaces, which cause the accumulation of charges that will dissipate EMW [45,46]. Besides, these interfaces can increase the wave propagation path and further attenuate EMW.

In addition, α is an important index of the EMA characteristic absorbers. Concurring to the hypothesis of transmission line, α can be calculated [47]:

$$\alpha = \frac{\sqrt{2}\pi f}{c} \times \sqrt{(\mu''\varepsilon'' - \mu'\varepsilon') + \sqrt{(\mu''\varepsilon'' - \mu'\varepsilon')^2 + (\mu'\varepsilon'' + \mu''\varepsilon')^2}} \quad (5)$$
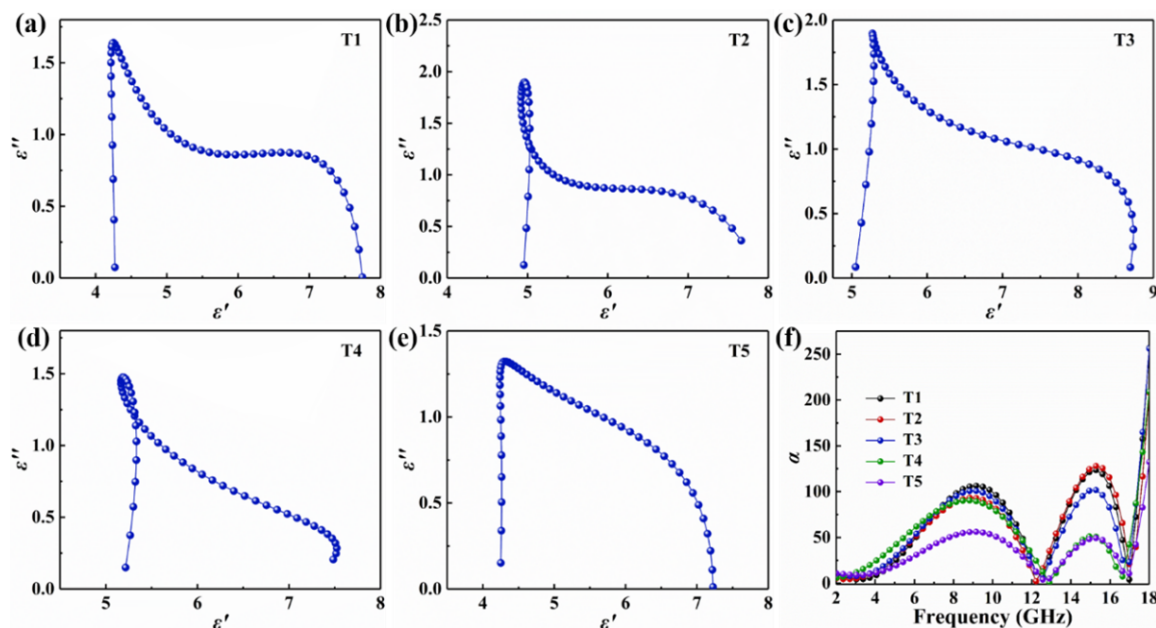
Fig. 8 Cole–Cole semicircles of (a) T1, (b) T2, (c) T3, (d) T4, and (e) T5. (f) Attenuation constants (α) of all samples.
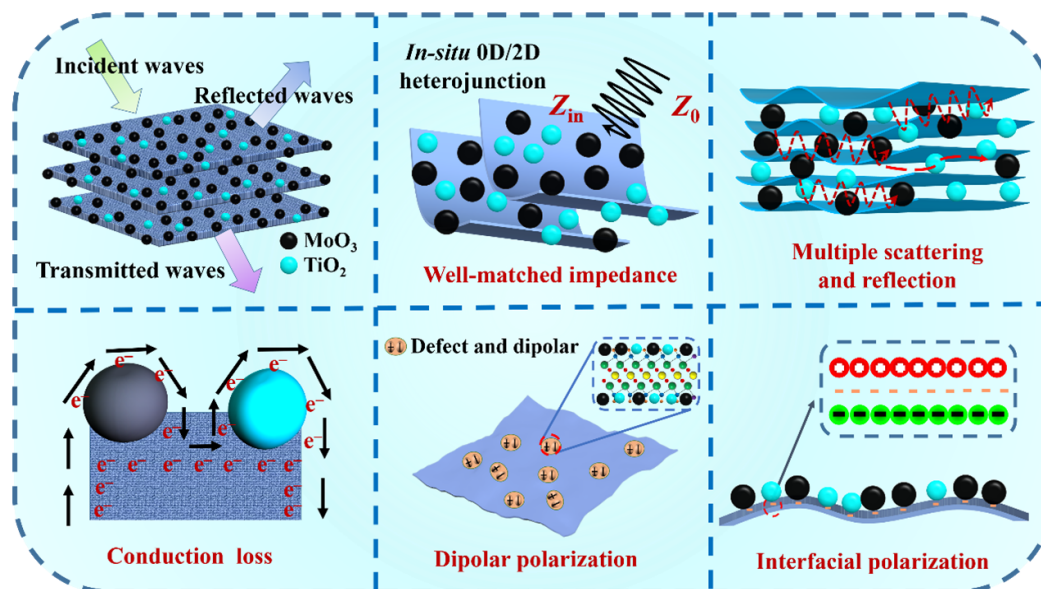

Fig. 9 Schematic illustration of the absorbing mechanism of $MoO_3/TiO_2/Mo_2TiC_2T_x$.

T3 can reach a maximum α value of 256 at 18 GHz, indicating its extremely high EMW attenuation capability (Fig. 8(f)).

In brief, the EMA mechanism of the layered $MoO_3/TiO_2/Mo_2TiC_2T_x$ obtained by the annealing of m-$Mo_2TiC_2T_x$ MXene is shown in Fig. 9. It can be summarized that the 0D/2D heterogeneous structure obtained by the annealing treatment optimizes the impedance matching situation of $Mo_2TiC_2T_x$ MXene, which makes it easier for EMW to enter the interior of the material. The conduction loss, dipolar polarization,

interfacial polarization relaxation, and multiple scattering and reflection of EMW by the laminar structure can effectively dissipate the incident waves.

4   Conclusions

In summary, m-$Mo_2TiC_2T_x$ was obtained by etching Mo_2TiAlC_2 with high concentration of HF, and the layered $MoO_3/TiO_2/Mo_2TiC_2T_x$ materials were prepared by the simple annealing treatment for $Mo_2TiC_2T_x$

MXene. The effects of different annealing temperatures on the structure, morphology, and microwave absorption properties of $MoO_3/TiO_2/Mo_2TiC_2T_x$ materials were studied. It was found that MoO_3 and TiO_2 oxide spheres uniformly grew among $MoO_3/TiO_2/Mo_2TiC_2T_x$ layers with increasing the annealing temperature and gradually increasing the particle size, enlarging the layer spacing of $Mo_2TiC_2T_x$ nanosheets. The layered $MoO_3/TiO_2/Mo_2TiC_2T_x$ hybrids treated at 300 ℃ exhibit a minimum RL_{min} value of −30.76 dB (2.3 mm) at 10.18 GHz with an ultra-broaden EAB of 8.6 GHz (1.8 mm). The analysis reveals that the good impedance matching situation, enhanced dielectric loss, and multiple scattering and reflection due to the 0D/2D structure are the main EMA mechanisms of the 2D MXene-based hybrids.

Acknowledgements

Declaration of competing interest

The authors have no competing interests to declare that are relevant to the content of this article.

Electronic Supplementary Material

Supplementary material is available in the online version of this article at https://doi.org/10.1007/s40145-022-0624-0.

References

[1] Ying MF, Zhao RZ, Hu X, *et al*. Wrinkled titanium carbide (MXene) with surface charge polarizations through chemical etching for superior electromagnetic interference shielding. *Angew Chem Int Ed* 2022, **61**: e202201323.

[2] Shui WC, Li JM, Wang H, *et al*. $Ti_3C_2T_x$ MXene sponge composite as broadband terahertz absorber. *Adv Opt Mater* 2020, **8**: 2001120.

[3] Wang YL, Wang GS, Zhang XJ, *et al*. Porous carbon polyhedrons coupled with bimetallic CoNi alloys for frequency selective wave absorption at ultralow filler loading. *J Mater Sci Technol* 2022, **103**: 34–41.

[4] Wang HY, Sun XB, Wang GS. A MXene-modulated 3D crosslinking network of hierarchical flower-like MOF derivatives towards ultra-efficient microwave absorption properties. *J Mater Chem A* 2021, **9**: 24571–24581.

[5] Li X, Wu ZC, You WB, *et al*. Self-assembly MXene-rGO/CoNi film with massive continuous heterointerfaces and enhanced magnetic coupling for superior microwave absorber. *Nano Micro Lett* 2022, **14**: 73.

[6] Qing YC, Zhou WC, Luo F, *et al*. Titanium carbide (MXene) nanosheets as promising microwave absorbers. *Ceram Int* 2016, **42**: 16412–16416.

[7] Liu ZH, Cui YH, Li Q, *et al*. Fabrication of folded $MXene/MoS_2$ composite microspheres with optimal composition and their microwave absorbing properties. *J Colloid Interface Sci* 2022, **607**: 633–644.

[8] Hou TQ, Jia ZR, Dong YH, *et al*. Layered 3D structure derived from MXene/magnetic carbon nanotubes for ultra-broadband electromagnetic wave absorption. *Chem Eng J* 2022, **431**: 133919.

[9] Yang ML, Yuan Y, Li Y, *et al*. Anisotropic electromagnetic absorption of aligned $Ti_3C_2T_x$ MXene/gelatin nanocomposite aerogels. *ACS Appl Mater Interfaces* 2020, **12**: 33128–33138.

[10] Li X, You WB, Wang L, *et al*. Self-assembly-magnetized MXene avoid dual-agglomeration with enhanced interfaces for strong microwave absorption through a tunable electromagnetic property. *ACS Appl Mater Interfaces* 2019, **11**: 44536–44544.

[11] Li X, Wen CY, Yang LT, *et al*. MXene/FeCo films with distinct and tunable electromagnetic wave absorption by morphology control and magnetic anisotropy. *Carbon* 2021, **175**: 509–518.

[12] Zhang C, Wu ZC, Xu CY, *et al*. Hierarchical $Ti_3C_2T_x$ MXene/carbon nanotubes hollow microsphere with confined magnetic nanospheres for broadband microwave absorption. *Small* 2022, **18**: 2104380.

[13] Hu FY, Wang XH, Niu HH, *et al*. Synthesis and electromagnetic wave absorption of novel $Mo_2TiC_2T_x$ MXene with diverse etching methods. *J Mater Sci* 2022, **57**: 7849–7862.

[14] Li XL, Yin XW, Han MK, *et al*. A controllable heterogeneous structure and electromagnetic wave absorption properties of Ti_2CT_x MXene. *J Mater Chem C* 2017, **5**: 7621–7628.

[15] Fan BB, Shang SY, Dai BZ, *et al*. 2D-layered Ti_3C_2/TiO_2 hybrids derived from Ti_3C_2 MXenes for enhanced electromagnetic wave absorption. *Ceram Int* 2020, **46**: 17085–17092.

[16] Wei Y, Zhang P, Soomro RA, *et al*. Advances in the synthesis of 2D MXenes. *Adv Mater* 2021, **33**: 2103148.

[17] Anasori B, Xie Y, Beidaghi M, *et al*. Two-dimensional, ordered, double transition metals carbides (MXenes). *ACS Nano* 2015, **9**: 9507–9516.

[18] Kim H, Anasori B, Gogotsi Y, *et al*. Thermoelectric

properties of two-dimensional molybdenum-based MXenes. *Chem Mater* 2017, **29**: 6472–6479.

[19] Gao YJ, Cao YY, Zhuo H, *et al*. Mo_2TiC_2 MXene: A promising catalyst for electrocatalytic ammonia synthesis. *Catal Today* 2020, **339**: 120–126.

[20] Anasori B, Dahlqvist M, Halim J, *et al*. Experimental and theoretical characterization of ordered MAX phases Mo_2TiAlC_2 and $Mo_2Ti_2AlC_3$. *J Appl Phys* 2015, **118**: 094304.

[21] Guo J, Zhao YY, liu AM, *et al*. Electrostatic self-assembly of 2D delaminated MXene (Ti_3C_2) onto Ni foam with superior electrochemical performance for supercapacitor. *Electrochimica Acta* 2019, **305**: 164–174.

[22] Maughan PA, Bouscarrat L, Seymour VR, *et al*. Pillared Mo_2TiC_2 MXene for high-power and long-life lithium and sodium-ion batteries. *Nanoscale Adv* 2021, **3**: 3145–3158.

[23] Zhang JQ, Zhao YF, Guo X, *et al*. Single platinum atoms immobilized on an MXene as an efficient catalyst for the hydrogen evolution reaction. *Nat Catal* 2018, **1**: 985–992.

[24] Hu FY, Wang XH, Bao S, *et al*. Tailoring electromagnetic responses of delaminated $Mo_2TiC_2T_x$ MXene through the decoration of Ni particles of different morphologies. *Chem Eng J* 2022, **440**: 135855.

[25] Wojciechowski T, Rozmysłowska-Wojciechowska A, Matyszczak G, *et al*. Ti_2C MXene modified with ceramic oxide and noble metal nanoparticles: Synthesis, morphostructural properties, and high photocatalytic activity. *Inorg Chem* 2019, **58**: 7602–7614.

[26] Sun XX, Li YB, Huang YX, *et al*. Achieving super broadband electromagnetic absorption by optimizing impedance match of rGO sponge metamaterials. *Adv Funct Mater* 2022, **32**: 2107508.

[27] Cao MS, Wang XX, Cao WQ, *et al*. Thermally driven transport and relaxation switching self-powered electromagnetic energy conversion. *Small* 2018, **14**: 1800987.

[28] Wang YL, Yang SH, Wang HY, *et al*. Hollow porous CoNi/C composite nanomaterials derived from MOFs for efficient and lightweight electromagnetic wave absorber. *Carbon* 2020, **167**: 485–494.

[29] Zhou CL, Wang XX, Luo H, *et al*. Interfacial design of sandwich-like $CoFe@Ti_3C_2T_x$ composites as high efficient microwave absorption materials. *Appl Surf Sci* 2019, **494**: 540–550.

[30] Sun CH, Jia ZR, Xu S, *et al*. Synergistic regulation of dielectric-magnetic dual-loss and triple heterointerface polarization via magnetic MXene for high-performance electromagnetic wave absorption. *J Mater Sci Technol* 2022, **113**: 128–137.

[31] Li X, You WB, Xu CY, *et al*. 3D seed-germination-like MXene with *in situ* growing CNTs/Ni heterojunction for enhanced microwave absorption via polarization and magnetization. *Nano-Micro Lett* 2021, **13**: 157.

[32] Dai Y, Wu XY, Liu ZS, *et al*. Highly sensitive, robust and anisotropic MXene aerogels for efficient broadband microwave absorption. *Compos Part B-Eng* 2020, **200**: 108263.

[33] Cui GZ, Sun XD, Zhang GY, *et al*. Electromagnetic absorption performance of two-dimensional MXene $Ti_3C_2T_x$ exfoliated by HCl+LiF etchant with diverse etching times. *Mater Lett* 2019, **252**: 8–10.

[34] Han MK, Yin XW, Wu H, *et al*. Ti_3C_2 MXenes with modified surface for high-performance electromagnetic absorption and shielding in the X-band. *ACS Appl Mater Interfaces* 2016, **8**: 21011–21019.

[35] Liang LY, Yang RS, Han GJ, *et al*. Enhanced electromagnetic wave-absorbing performance of magnetic nanoparticles-anchored 2D $Ti_3C_2T_x$ MXene. *ACS Appl Mater Interfaces* 2020, **12**: 2644–2654.

[36] Du H, Zhang QP, Zhao B, *et al*. Novel hierarchical structure of $MoS_2/TiO_2/Ti_3C_2T_x$ composites for dramatically enhanced electromagnetic absorbing properties. *J Adv Ceram* 2021, **10**: 1042–1051.

[37] Chang M, Jia ZR, He SQ, *et al*. Two-dimensional interface engineering of $NiS/MoS_2/Ti_3C_2T_x$ heterostructures for promoting electromagnetic wave absorption capability. *Compos Part B-Eng* 2021, **225**: 109306.

[38] Gao Y, Du H, Li RR, *et al*. Multi-phase heterostructures of flower-like Ni(NiO) decorated on two-dimensional $Ti_3C_2T_x/TiO_2$ for high-performance microwave absorption properties. *Ceram Int* 2021, **47**: 10764–10772.

[39] Wang BJ, Li SK, Huang FZ, *et al*. Construction of multiple electron transfer paths in 1D core–shell hetetrostructures with MXene as interlayer enabling efficient microwave absorption. *Carbon* 2022, **187**: 56–66.

[40] Liang LL, Gu WH, Wu Y, *et al*. Heterointerface engineering in electromagnetic absorbers: New insights and opportunities. *Adv Mater* 2022, **34**: 2106195.

[41] Hou YL, Sheng ZZ, Fu C, *et al*. Hygroscopic holey graphene aerogel fibers enable highly efficient moisture capture, heat allocation and microwave absorption. *Nat Commun* 2022, **13**: 1227.

[42] Zhu M, Yan XX, Xu HL, *et al*. Ultralight, compressible, and anisotropic MXene@wood nanocomposite aerogel with excellent electromagnetic wave shielding and absorbing properties at different directions. *Carbon* 2021, **182**: 806–814.

[43] Liu W, Tan SJ, Yang ZH, *et al*. Hollow graphite spheres embedded in porous amorphous carbon matrices as lightweight and low-frequency microwave absorbing material through modulating dielectric loss. *Carbon* 2018, **138**: 143–153.

[44] Wang F, Gu WH, Chen JB, *et al*. The point defect and electronic structure of K doped $LaCo_{0.9}Fe_{0.1}O_3$ perovskite with enhanced microwave absorbing ability. *Nano Res* 2022, **15**: 3720–3728.

[45] Liu QH, Cao Q, Bi H, *et al*. $CoNi@SiO_2@TiO_2$ and $CoNi@Air@TiO_2$ microspheres with strong wideband microwave absorption. *Adv Mater* 2016, **28**: 486–490.

[46] Sun H, Che RC, You X, *et al*. Cross-stacking aligned carbon-nanotube films to tune microwave absorption frequencies and increase absorption intensities. *Adv Mater* 2014, **26**: 8120–8125.

[47] Du B, Cai M, Wang X, *et al*. Enhanced electromagnetic

wave absorption property of binary ZnO/NiCo$_2$O$_4$ composites. *J Adv Ceram* 2021, **10**: 832–842.